A&A 675, A170 (2023)
https://doi.org/10.1051/0004-6361/202346623

Astronomy & Astrophysics
Special issue

Solar Orbiter First Results (Nominal Mission Phase)

Recurrent solar density transients in the slow wind observed with the Metis coronagraph★

R. Ventura[1], E. Antonucci[2], C. Downs[3], P. Romano[1], R. Susino[2], D. Spadaro[1], D. Telloni[2], S. L. Guglielmino[1], G. Capuano[1], V. Andretta[4], F. Landini[2], G. Jerse[5], G. Nicolini[2], M. Pancrazzi[2], C. Sasso[4], V. Da Deppo[6], S. Fineschi[2], C. Grimani[7,8], P. Heinzel[9,10], D. Moses[11], G. Naletto[12], M. Romoli[13], M. Stangalini[14], L. Teriaca[15], and M. Uslenghi[16]

[1] INAF-Catania Astrophysical Observatory, Via S. Sofia 78, 95123 Catania, Italy
e-mail: rita.ventura@inaf.it
[2] INAF-Turin Astrophysical Observatory, Via Osservatorio 20, 10025 Pino Torinese (TO), Italy
[3] Predictive Science Inc., 9990 Mesa Rim Rd., 92121 San Diego, CA, USA
[4] INAF – Astronomical Observatory of Capodimonte, Salita Moiariello 16, 80131 Naples, Italy
[5] INAF – Trieste Astronomical Observatory, Via Giambattista Tiepolo 11, 34149 Trieste, Italy
[6] CNR – Institute for Photonics and Nanotechnologies, Via Trasea 7, 35131 Padua, Italy
[7] University of Urbino Carlo Bo, Department of Pure and Applied Sciences, Via Santa Chiara 27, 61029 Urbino, Italy
[8] National Institute for Nuclear Physics, Section in Florence, Via Bruno Rossi 1, 50019 Sesto Fiorentino, Italy
[9] Czech Academy of Sciences, Astronomical Institute, Fričova 298, 25165 Ondřejov, Czech Republic
[10] University of Wrocław, Centre of Scientific Excellence – Solar and Stellar Activity, ul. Kopernika 11, 51-622 Wrocław, Poland
[11] National Aeronautics and Space Administration, Headquarters, Washington, DC 20546, USA
[12] University of Padua, Department of Physics and Astronomy, Via Francesco Marzolo 8, 35131 Padova, Italy
[13] University of Florence, Department of Physics and Astronomy, Via Giovanni Sansone 1, 50019 Sesto Fiorentino, Italy
[14] Italian Space Agency, Via del Politecnico snc, 00133 Roma, Italy
[15] Max Planck Institute for Solar System Research, Justus-von-LiebigWeg 3, 37077 Göttingen, Germany
[16] National Institute for Astrophysics, Institute of Space Astrophysics and Cosmic Physics of Milan, Via Alfonso Corti 12, 20133 Milano, Italy

Received 7 April 2023 / Accepted 25 May 2023

ABSTRACT

Aims We aim to investigate and characterize the morphology and dynamics of small-scale coronal plasma density inhomogeneities detected as brighter, denser features propagating outward through the solar corona in the visible-light images of the Metis coronagraph on board Solar Orbiter on February 22, 2021. Our main focus is on investigating their possible origin and contribution to the slow wind variability and dynamics and their dependence on coronal magnetic field configurations and structure.
Methods. The method adopted is based on the computations of autocorrelation and cross-correlation functions applied to temporal and spatial series of total brightness as a function of the heliocentric distance and solar latitudes.
Results. We find that the plasma density inhomogeneities studied here are small-scale structures with typical radial and transverse sizes, as projected on the plane of sky, on the order of 500 Mm and 40 Mm, respectively, and that they are up to 24 times brighter than the ambient solar wind. The brighter density structures exhibit longer lifetime and more stable shape and dimensions as they travel toward the outer edge of the field of view. The enhanced density structures are ejected with a most probable cadence of about 80 min at or below the inner edge of the Metis field of view (within 3.1 $R_\odot$–5.7 $R_\odot$ at the time of observations) in a wide latitudinal region corresponding to the site of a complex web of separatrix and quasi-separatrix layers, as resulting from the simulated magnetohydrodynamic configuration of the west limb of the solar corona. Some of the moving density enhancements clearly show morphological characteristics compatible with the switchback phenomenon, supporting the results indicating that the switchbacks occur at the coronal level. The enhanced density structures were ejected into the ambient slow wind with a mean velocity of about 240 ± 40 km s^{-1}, which is significantly higher than that deduced for the ambient solar wind on the basis of previous Metis observations during the solar minimum of cycle 24. The absence of acceleration observed across the coronagraph field of view suggests that the ejected plasmoids are progressively reaching the expansion rate of the ambient wind.
Conclusions. The results suggest that the quasi-periodic enhanced-density plasmoids might be the consequence of reconnection phenomena occurring in the complex web of the separatrix and quasi-separatrix layers present in the solar corona. Moreover, the structural characteristics of some of the detected plasmoids are in favor of the presence of switchbacks that originate during interchange reconnection processes occurring at or below 3 $R_\odot$ in the S-web. The speed of the plasma ejected in the reconnection process is higher than that of the ambient slow solar wind and is likely to be related to the energy involved in the process generating the propagating structures.

Key words. Sun: corona – solar wind – magnetohydrodynamics (MHD) – magnetic reconnection – techniques: image processing

★ Movie associated to Figs. 1 and 11 is available at https://www.aanda.org

1. Introduction

During the past decades, theoretical studies, remote sensing observations of the solar wind in the outer corona, and in situ measurements in the heliosphere have been devoted to understanding the fundamental physical processes responsible for the solar wind formation, heating, and acceleration. It is well known that two regimes of solar wind with distinctly different plasma properties and different origins coexist: the fast wind and the slow wind (e.g., McComas et al. 2008). While the fast solar wind originates in the core of coronal holes where the magnetic field lines are locally open, letting the coronal plasma flow out into the interplanetary medium, the question of the source regions of the slow solar wind is still under debate (see e.g., Antiochos et al. 2012; Antonucci et al. 2012, 2020a, 2023; Abbo et al. 2016; Wang 2012, 2020; Cranmer et al. 2017; Viall & Borovsky 2020). Since the 1970s, visible-light observations and in situ heliospheric plasma data have demonstrated that the slow solar wind is highly structured at many temporal and spatial scales showing high variability in plasma physical parameters, such as magnetic field, velocity, density, chemical composition, and charge state (see e.g., Buergi & Geiss 1986; McComas et al. 1998; Zurbuchen et al. 1999, 2002; Gloeckler et al. 2003; Gershkovich et al. 2022). An accurate determination of the temporal and spatial scales characterizing the detected variability is essential to providing stringent constraints on theoretical modeling.

A recent study of the first observation of the solar wind obtained on May 2020 with the Metis visible-light and ultraviolet coronagraph (Antonucci et al. 2020b; Fineschi et al. 2020) on board Solar Orbiter (Müller 2020), analyzed in the context of the plasma configuration resulting from a 3D magnetohydrodynamic (MHD) model of the solar corona, has provided an accurate characterization of the slow wind belt in the outer solar atmosphere during the quiescent phase of the solar cycle (Antonucci et al. 2023). The slow wind was detected in a latitude zone within ±30° around the coronal segment of the heliospheric current sheet dividing opposite magnetic polarities. In the absence of detectable transient phenomena, such as large-scale coronal mass ejections (CMEs) or smaller scale plasmoids detaching close to the cusp of coronal streamers and propagating along the current sheet (Sheeley et al. 1997; Wang & Sheeley 1998; Wang 2012; Wang et al. 2000; Sanchez-Diaz et al. 2017), the quasi-steady slow wind flow is regulated – as expected – by the divergence of the open magnetic field lines surrounding the equatorial streamer. The slow wind belt, however, is also the region where open magnetic field corridors characteristic of the separatrices and quasi-separatrices, forming a web (i.e., S-web) near coronal hole-streamer boundaries, are present. Reconnection along the separatrices has been proposed as an efficient mechanism for explaining the origin and acceleration of the slow wind (Antiochos et al. 2011, 2012). Indeed, recent extreme ultraviolet (EUV) imaging observations revealed a spatially complex web of magnetized plasma structures that persistently interact and reconnect in the middle corona, which appears to be directly linked to the topological structure of the S-web (Chitta et al. 2023). The plasma released in the corona can also assume the form of magnetic switchbacks due to interchange reconnection between open and closed field lines (Telloni et al. 2022). Regarding this connection, it is worth noting that the solar wind study by Antonucci et al. (2023) shows that the S-web is enhanced in coincidence with the slow wind belt. The present analysis is based on data acquired in February 2021 during low coronal activity and over an observational interval longer than the time interval analyzed by Antonucci et al. (2023). Our aim is to complement the quasi-steady slow wind study by focusing on the contribution of the non-steady sources that can assure the observed variability of the slow wind physical parameters with transient ejections of plasma.

In addition to the CME events, which are frequently associated with magnetic reconnection at the cusp of the streamers where the current sheet originates, observations have repeatedly shown evidence of smaller scale plasmoids, the so-called blobs, which appear to be injected in the ambient slow solar wind along the current sheet and are likely associated with flux ropes ejected at the tip of the helmet streamers with a typical cadence of four to six per day (Wang & Sheeley 1998; Sheeley et al. 1999; Song et al. 2009). Together with the CMEs and blobs, frequent, quasi-periodic small-scale density inhomogeneities have been observed over a wide latitude range of the corona and are easily identifiable in the heliospheric medium (Sheeley et al. 1997; Wang & Sheeley 1998; Song et al. 2009; Viall & Vourlidas 2015; Abbo et al. 2016; Kepko et al. 2016, 2020; DeForest et al. 2018; Viall et al. 2021). Quasi-periodic density inhomogeneities of mesoscale size have been seen in visible-light coronal images obtained with various instruments on board the Solar and Heliospheric Observatory (SOHO; Domingo et al. 1995) and the Solar TErrestrial RELations Observatory (STEREO; Kaiser 2005) satellites. These structures enter the coronagraph fields of view (FOVs) and propagate outwards at nearly all ranges of the heliocentric distances covered by the instruments, with a characteristic cadence ranging from tens of minutes to several hours and typical sizes from 100 to 1000 Mm (0.14–1.4 $R_\odot$). Density structures have also been detected by in situ instruments up to 1 au (Di Matteo et al. 2019; Kepko et al. 2020), with timescales ranging from a few minutes to a couple of hours. Theoretical simulations recently performed by Réville et al. (2020) showed that the magnetic reconnection mechanism, triggered in certain physical conditions by the tearing-mode instability and capable of controlling the release of flux ropes, is successful in reproducing both the 1–2 h and 10–20 h ranges of the plasma inhomogeneities timescales. Studies of the coronal density structures, as part of the slow wind release and dynamics processes, are expected to cast light on the slow wind formation and acceleration, providing further diagnostic tools to take steps toward the solution of the slow solar wind puzzle.

In this paper, the results of the analysis of a sequence of visible-light images acquired with the Metis coronagraph during the Solar Orbiter cruise phase when the spacecraft was at 0.52 au from the Sun are presented. At that epoch, the solar activity was in the early ascending phase of cycle 25, and the corona still maintained a relatively simple configuration. During these observations, frequent, intermittent, and brighter, denser features entering the coronagraph FOV were detected predominantly in a wide mid and low latitude zone that includes the heliospheric current sheet. The observed plasma inhomogeneities and their propagation are studied in the context of a 3D MHD model of the solar corona.

The present paper can be considered as a preview and methodology test of planned extensive analyses of a longer (10 h) sequence of images acquired with Metis during the perihelion phase of October 2022 with higher temporal (2 min) and spatial (down to 4000 km) resolutions in an FOV (inner edge at about 1.7 $R_\odot$) where localized plasma density enhancements have been detected in the past with the COR1 coronagraph (Thompson et al. 2003) and the Extreme Ultraviolet Imager (EUVI; Wuelser et al. 2004) on board the STEREO

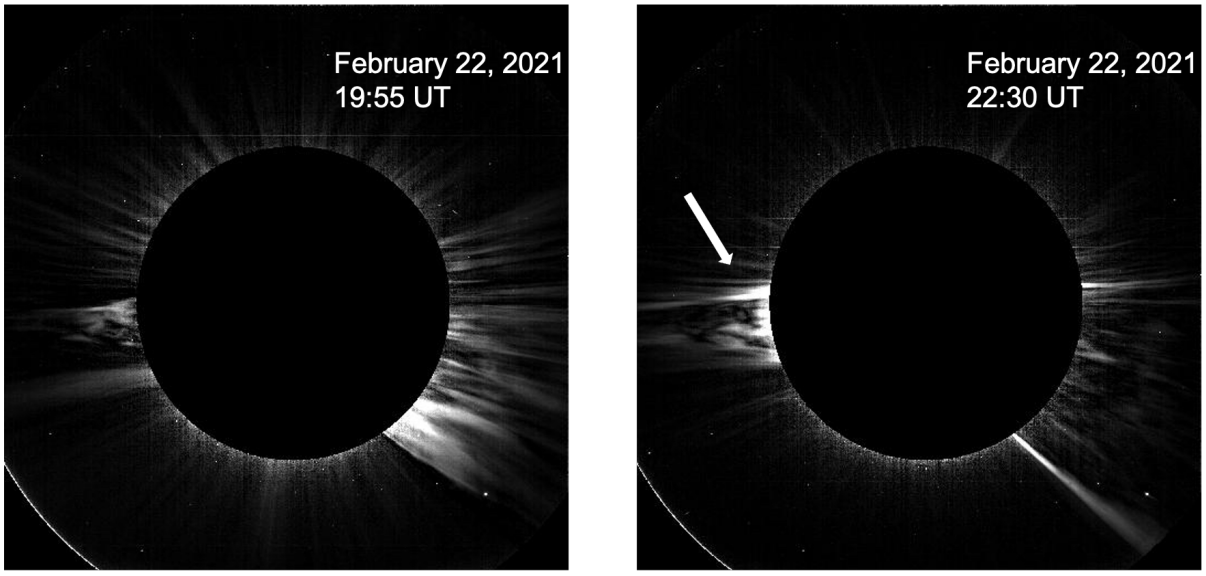

Fig. 1. Metis visible-light total brightness images of the solar corona on February 22, 2021, at 19:55 UT (left panel) and 22:30 UT (right panel) in the FOV 3.1 $R_\odot$–5.7 $R_\odot$ after subtraction of the minimum background image. In the right panel, a CME that started at about 20:50 UT is clearly visible above the east limb of the Sun and an arrow points out the CME's location. The temporal evolution of the full frames of the Metis observation sequence is available as an online movie.

satellite (Jones & Davila 2009; Alzate et al. 2021, 2023). Metis observations at the time of its close approach (0.29 au from the Sun) of October 2022 will provide better insight into the origin and dynamics of the outward-moving density enhancements observed at low heights in the solar corona thanks to their higher spatial and temporal resolutions. During the acquisition of the images, a large CME perturbed the magnetic configuration of the streamer belt at the east limb of the solar corona. For this reason, the most significant results have been obtained from observations of the area above the west limb. The method adopted is based on the computations of autocorrelation and cross-correlation functions applied to temporal and spatial series of total brightness collected with the Metis coronagraph as a function of the heliocentric distance and solar latitude. The paper is organized as follows. In Sect. 2, we describe in detail the observations and the data preprocessing applied, and we present the method of analysis and the results obtained in Sect. 3. We discuss the results in Sect. 4 and the conclusions we drew from the analysis in Sect. 5.

2. Observations and data preprocessing

During the Solar Orbiter cruise phase on February 22, 2021, when the spacecraft was at a distance of 0.52 au from the Sun (helio-latitude = 1.89° north relative to the solar equatorial plane and Carrington longitude = 162.48°), the Metis coronagraph acquired a series of visible-light images of the solar corona in the wavelength band of 580–640 nm. The corresponding FOV at that distance ranges from 3.1 $R_\odot$ (the internal occulter edge) up to 5.7 $R_\odot$. The observing sequence started at 19:55 UT and ended at 22:50 UT and had a cadence of 5 min. The plate scale was 10.7 arcsec pixel^{-1}, which at the distance of the spacecraft from the Sun at the time of the observations, corresponds to a spatial scale on the plane of the sky (POS) of about 16 Mm pixel^{-1} (0.02 $R_\odot$ pixel^{-1}), since the images were acquired with a 4 × 4 pixel^2 binning. The images (512 × 512 pixel^2) were processed and calibrated following the procedure described in Romoli et al. (2021) and, for example, in Appendix A of Andretta et al. (2021). The intensity radiation data acquired during a rapid polarization sequence at polarization angles 0°, 45°, 90°, and 135° were properly combined (see Liberatore et al. 2023 for a detailed description of the procedure) in order to obtain a sequence of 36 visible-light polarized brightness (pB) and total brightness (tB) images calibrated to the mean solar disk brightness $B_\odot$.

A minimum background total brightness image was obtained by taking the minimum brightness in each pixel over the 36 acquired images. This minimum background image was then subtracted from each frame of total brightness. This procedure mainly removes the contributions coming from the F-corona, contributions due to scattered photospheric light by dust grains, the instrumental scattered light, and the fraction of the K-corona, which is globally produced by Thomson scattering by free electrons, that remains constant over the full observing run. The procedure described above highlights the dynamic transient features of the K-corona. It can be argued that the removal of the F-corona could be avoided by analyzing the polarized brightness images rather than the total brightness counterparts. However, typical signal-to-noise ratios in polarized brightness images are lower by about 30%–40% – at best for highly polarized structures – with respect to the signal-to-noise ratios of the corresponding total brightness images (S. Fineschi, priv. comm.).

Figure 1 shows the total brightness images of the solar corona observed with Metis on February 22, 2021, at 19:55 UT and 22:30 UT. In the frame acquired at 22:30 UT, a CME is clearly visible above the east limb of the solar corona (see arrow in the right panel of Fig. 1).

In order to explore the morphological and dynamic characteristics of the density structures injected into the ambient slow solar wind and to assess their dependence on the heliocentric distance and latitude, we analyzed the Metis total brightness in ten concentric annuli in the range of 3.14–5.52 $R_\odot$, 0.22 $R_\odot$ wide, and spaced by 0.02 $R_\odot$ and located at increasingly higher heliocentric distances along 24 radial directions separated by 15° from each other. Table 1 reports the inner and outer edges (in solar radius units) of each annulus.

Table 1. Inner and outer edges of the ten selected annuli.

N. annulus	Inner radius $R_\odot$	Outer radius $R_\odot$
1	3.14	3.36
2	3.38	3.60
3	3.62	3.84
4	3.86	4.08
5	4.10	4.32
6	4.34	4.56
7	4.58	4.80
8	4.82	5.04
9	5.06	5.28
10	5.30	5.52

For each annulus and radial direction, we averaged the total brightness over all pixels inside the annulus itself at a given latitude. We reiterated the procedure for each of the 36 images in the observational sequence, resulting in a time series of average total brightness as a function of time, heliocentric distance, and radial direction. We standardized each time series, normalizing the data to zero mean and unit standard deviation in order to transform all values to a comparable scale.

In Fig. 2, the maps of the total brightness time series are reported as a function of time and heliocentric distance for the 24 radial directions we examined. Each panel refers to a different radial direction, expressed in terms of polar angle (PA) values measured counterclockwise from the north pole.

As shown in Fig. 2, bright diagonal traces due to localized plasma density enhancements moving outward are evident in the region between PA = 285°–240° (15° north and 30° south relative to the equator). In a wider range (out to PA = 315° and 210°), it is still possible to note the flows of outward-moving features, although they are fainter and thus less easily identifiable. Beyond these latitudes, the total brightness intensity appears to be purely randomly distributed.

This picture suggests that the region preferentially affected by the formation and propagation of frequent outward-moving density structures that are ultimately ejected below the inner edge of the Metis FOV ($3.14\,R_\odot$) corresponds to the latitude belt where the slow solar wind is generally confined when the solar activity is low (±30° from the equatorial streamer at solar minimum, as discussed in Antonucci et al. 2023). It is worth noting that at the east equator, the occurrence of a CME during the Metis observations disrupted the ambient magnetic configuration regulating the morphology and dynamics of the region (see right panel of Fig. 1). As a consequence, during the CME event, lasting for most of the Metis observing time, the maps of total brightness referring to the sector around the east equator do not show any evidence of ejected plasma flowing at the spatial scales observed at the opposite limb.

The region where the outward-propagating structures can be better identified includes the current sheet forming as an extension of a well-defined streamer lying at PA = 275°, which is slightly north of the equatorial plane, and reaches to the latitude of the plasma sheet formed as an extension of a pseudostreamer present in the southern hemisphere at PA = 236° (34° south of the equator), as shown in Figs. 3 and 4. Another pseudostreamer is present at PA ≃ 300°.

In Fig. 3, the map of the polarized brightness of the solar corona obtained with Metis on February 22, 2021, at 19:55 UT is compared with that resulting from 3D MHD simulations using magnetic boundary conditions derived from measurements made by the Helioseismic and Magnetic Imager on the Solar Dynamic Observatory (SDO/HMI; Scherrer et al. 2012). The model of the global corona used here is the thermodynamic MHD model, MAS, developed by Predictive Science Inc. (Lionello et al. 2009; Mikić et al. 2018). This model uses a wave-turbulence-driven (WTD) approach to specify coronal heating (see Mikić et al. (2018) for a description of the 3D implementation and Boe et al. (2021, 2022) for a benchmark of the exact WTD model parameterization used here). The choice of the full-Sun magnetic data used to model the corona was optimized to better reflect the conditions at the time of the Metis west limb observations. The data selected to define the boundary conditions include the HMI radial magnetic field from synoptic maps for the Carrington rotations CRs 2240 and 2241. To improve the accuracy of the model beneath the west limb of Solar Orbiter at this time, the radial field derived from the full-disk 720s HMI vector magnetogram on February 22 at 22:50 UT was used to replace the synoptic data in a patch from approximately 270° to 320° Carrington longitude and ± 30° latitude. This composite magnetic map was then pole-filled in and smoothed to the model resolution (as in e.g., Mikić et al. 2018; Boe et al. 2021; Telloni et al. 2022).

The brightest, better identified density structures were observed in the regions where the slow solar wind is expected to originate. These transients were ejected at a heliocentric distance below or around $3.14\,R_\odot$ (inner edge of the Metis FOV) and propagated in a region where, according to the MHD simulations, the magnetic field lines are fully open and extend radially outward beyond $3\,R_\odot$, as can be seen in Fig. 4.

3. Analysis of the coronal density structures

The region where the full-frame sequence of the Metis images (Fig. 1) and the total brightness maps, constructed in the preprocessing analysis phase (Fig. 2), show the preferential detection of the density structures (i.e., at the west limb of the corona between PA = 285° and 240°) was further studied by adopting a finer latitudinal sampling of 2°, selecting additional radial directions, and deriving the corresponding maps of total brightness time series. The most representative example is reported in Fig. 5, where the map of the total brightness intensity as a function of the observation time and the heliocentric distance is shown for the radial direction at PA = 263°. Three density features (labeled as A, B, and C) entering the FOV of the Metis coronagraph at quasi-regular time intervals and forming a running train of structures moving outward are clearly visible as diagonal bands in Fig. 5.

3.1. General characteristics

Some relevant characteristics of the morphology, temporal evolution, and ensemble properties of the density structures identified in the Metis FOV can be derived from a simple inspection of Fig. 5. These include the maximum density ratio between the brightest structures and the mean background slow wind level, their spatial scales (deduced from the radial extension of maxima along the radial distance-axis direction), the source location, the lifetime, the cadence of plasma release (from the succession of maxima and minima – annulus by annulus – in the time-axis direction), and the flow speed of the structures projected on the POS by comparing the succession of maxima and minima in the

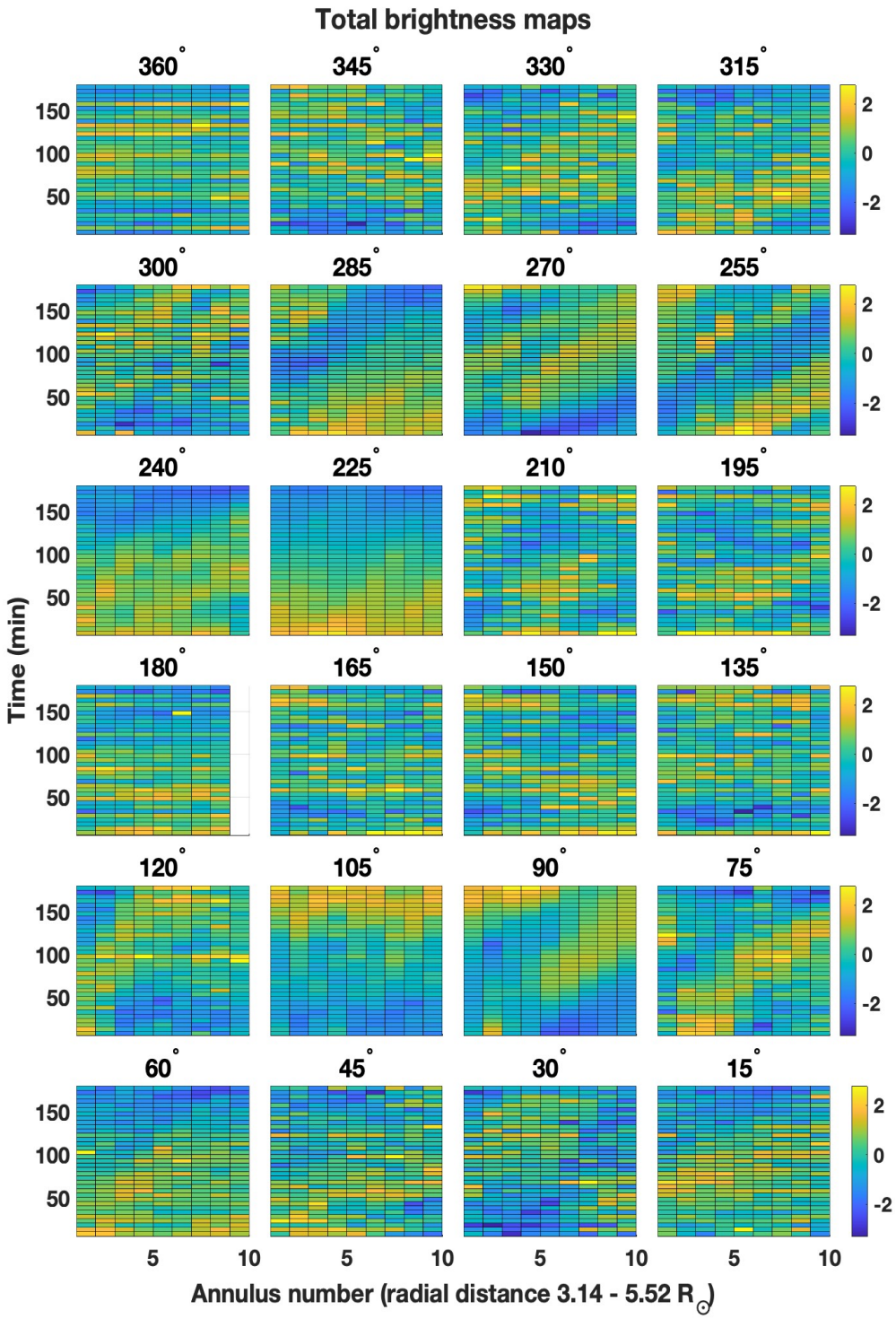

Fig. 2. Maps of total brightness intensity as a function of time and heliocentric distance for the 24 radial directions considered in the analysis. Each time series of total brightness was normalized to zero mean and unit standard deviation. The radial directions are indicated at the top of the corresponding panel in terms of the PA value, measured counterclockwise from the north pole. In the map referring to PA = 180°, the data corresponding to the tenth annulus are missing since they were outside the Metis FOV.

radial distance-axis direction at a given instant with those at subsequent times.

The density structures differ from each other in brightness, shape, radial and transverse extent, and lifetime. The maximum total brightness intensity is about 20 to 24 times higher than the background slow wind emission level. The typical spatial scales as projected on the POS are of the order of 0.7 $R_\odot$, equivalent to 500 Mm (see. e.g., Figs. 2 and 5). This confirms previous inferences that describe such structures as having mesoscale dimensions (e.g., Viall et al. 2010, 2021; Viall & Vourlidas 2015; Kepko et al. 2020). Typical ratios between transverse and radial scales are on the order of 8%.

The lifetimes vary in a large range, from about 1h 15m to 3h. The higher limit corresponds to the observational time

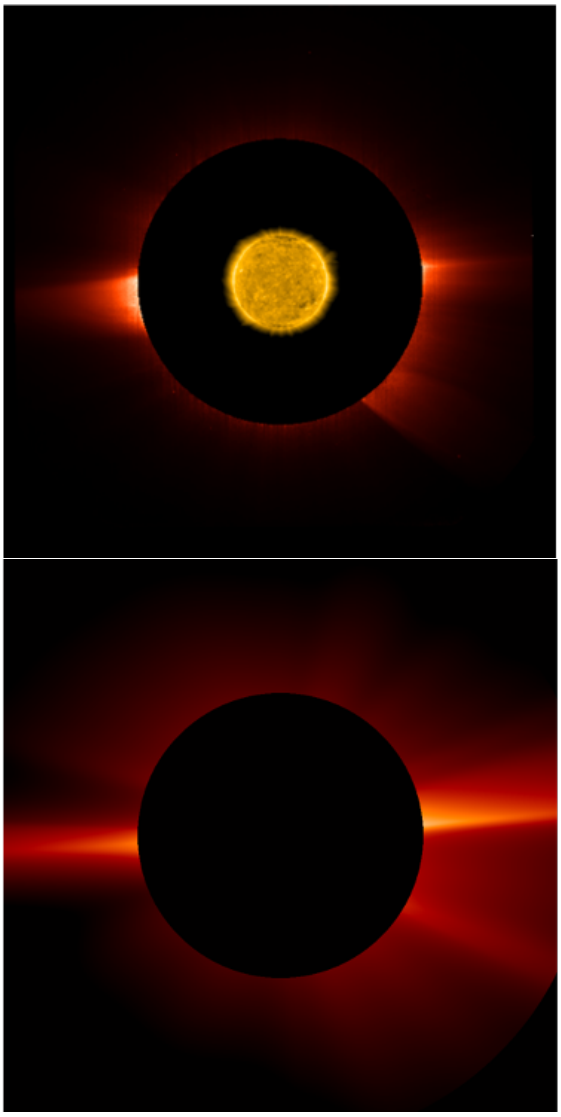

Fig. 3. Polarized brightness of the corona observed with Metis. Top panel: Map of the polarized brightness of the solar corona observed with Metis on February 22, 2021, at 19:55 UT within the FOV ranging from 3.1 $R_\odot$ to 5.7 $R_\odot$ combined with the solar disk emission at 17.4 nm observed with the Extreme Ultraviolet Imager on board Solar Orbiter (Rochus et al. 2020). Bottom panel: Radially filtered polarized brightness of the solar corona in the Metis FOV resulting from the Predictive Science Inc. 3D MHD simulations based on SDO/HMI measurements and calculated considering the position of the Solar Orbiter with respect to the Sun during the Metis observations.

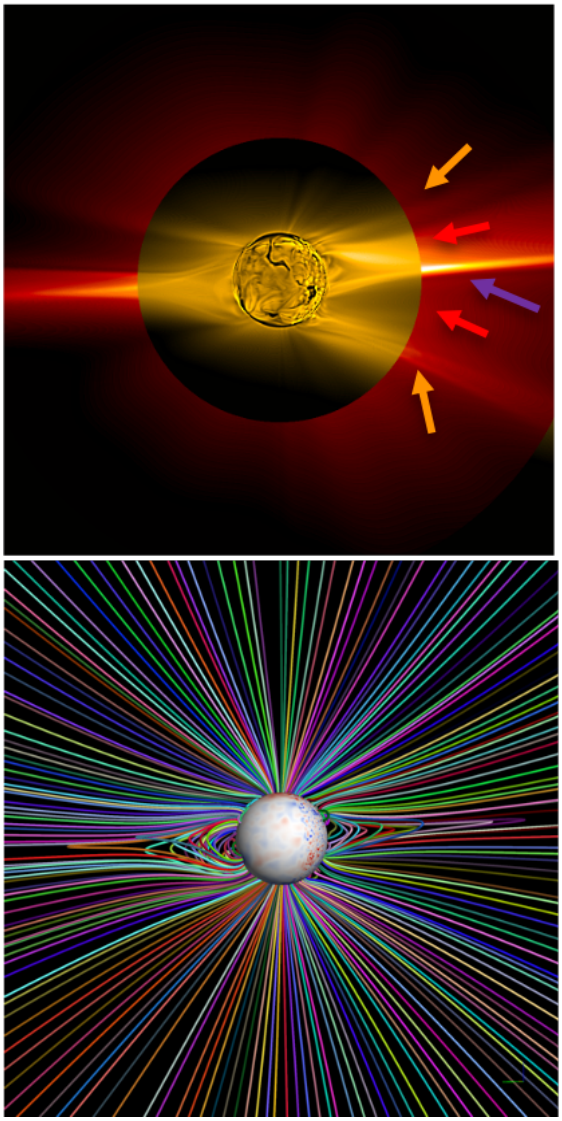

Fig. 4. Comparison of the observed and modeled polarized brightness of the corona. Top panel: Radially filtered polarized brightness of the solar corona from the limb to the outer edge of the Metis FOV resulting from the Predictive Science Inc. 3D MHD simulations computed to reflect the limb view of Metis. The polarized brightness image was combined with the Atmospheric Imaging Assembly on the Solar Dynamics Observatory (Lemen et al. 2012) observations of the 17.1 nm EUV emission. The blue arrow indicates the streamer, the orange arrows show the pseudostreamers, and the red arrows indicate the regions of the wind emanating from the coronal hole extensions (same color code as in Fig. 10). Bottom panel: Magnetic field lines traced on the POS on the basis of the 3D MHD model of the corona.

interval and is then the measurable lifetime lower limit for the most persistent features.

A mutual relation among the main properties of the coronal density structures emerged from the analysis. For example, the brighter the density structures, the longer the lifetime and more stable the shape and dimensions are as they travel toward the outer edge of the FOV (e.g., see density structure labeled B in Fig. 5).

The coronal features showing a lower brightness contrast (see e.g., Fig. 2, third panel, second row, PA = 270°) are those that change significantly in shape and dimensions and eventually elongate and fray, and they sometimes even completely dissolve before reaching the outer edge of the FOV. Some of the plasmoids in Fig. 2 are wave-shaped and appear to move in a non-radial direction so that they disappear at a given radial direction and reappear along another radial direction at a higher heliocentric distance, miming a new formation at a higher height (see e.g., third panel, second row – PA = 270° – of Fig. 2 where a density structure is seen entering the FOV at 4 $R_\odot$ 30 min after the start of the observation).

3.2. Density structure periodicities

For a more quantitative evaluation of all the parameters characterizing the transient inhomogenieties, we applied a data analysis approach based on autocorrelation and cross-correlation function computations. Within a latitude range of 45° wide where

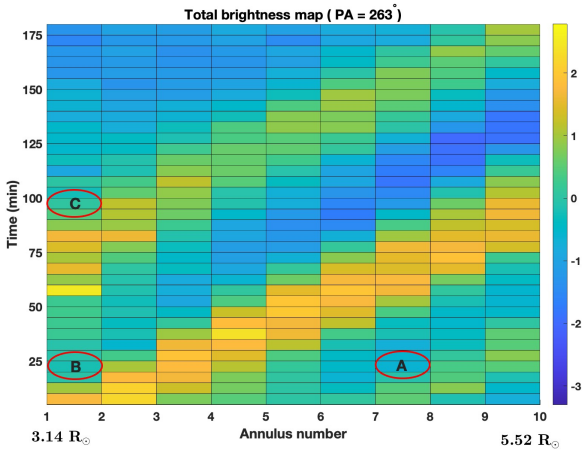

Fig. 5. Map of total brightness intensity as a function of time and heliocentric distance for the polar angle PA = 263°. Each time series of total brightness was normalized to zero mean and unit standard deviation. The labels A, B, and C indicate three different coronal density structures crossing the Metis FOV during the observing interval.

all the structures are more easily identifiable, approximately ten events were observed in about 3 h. In order to more accurately determine the cadence of the release of the density structures, autocorrelations of the total brightness time series were computed for each annulus in the range of PAs between 285° and 240°. Figure 6 shows, as a representative example, the results obtained for PA = 263°.

In addition to the obvious first maximum centered at zero lag, Fig. 6 shows that a significant periodicity with a peak value ranging between 75 and 90 min is present in all the time series analyzed, except the series relative to the first annulus and the series that refers to the second annulus where the periodicity is barely distinguishable. One more periodicity is present in the range of 125–150 min, with a peak value centered at 135 min in the time series relative to annulus 10. These correlations suggest that the release of the brighter structures crossing the Metis FOV is periodic or quasi-periodic. This result confirms previous similar studies on the solar corona density fluctuations in the literature (e.g., Viall et al. 2010; Viall & Vourlidas 2015).

The autocorrelation analysis results were verified by a Fourier analysis performed for each time series between 3.14 $R_\odot$ and 5.52 $R_\odot$ at a PA of 263°. Figures 7 shows, as an example, the normalized Lomb-Scargle periodogram (Scargle 1982) computed at 3.73 $R_\odot$ (annulus 3) and PA = 263°. A highly significant maximum (>99.9%) corresponding to a period of 83 min is predominant in the spectrum.

3.3. Density structure propagation speed

Following the same methodology of our analysis, we applied cross-correlations to the total brightness coronal emission to estimate the average speed and acceleration (if any) of the density structures moving outward across the Metis FOV. We cross-correlated the spatial series representing the variation of the total brightness intensity as a function of heliodistance along a radial direction (e.g., horizontal lines in Fig. 5) at a given time, with the analogous series along the same radial direction obtained at successive times. As an example, Fig. 8 shows the results obtained for the density structure labeled B in Fig. 5. We find it is worth noting that the feature labeled C in Fig. 5 shows the same time-radial distance profile and slope of the structure labeled B. The autocorrelation function of the radial series at PA= 263° at instant t_1 (top-left panel) is shown as a useful benchmark to guide the interpretation of the cross-correlation functions obtained by correlating this first radial series with those at increasing time delays t_n, which are plotted in the other panels. We considered the first 95 min of observation since afterward the density structure named B moved out of the FOV (see Fig. 5).

The most evident result obtained by comparing the shifts of the maximum value of the cross-correlation functions in each panel is that within the latitude range under study, the density structures travel radially across the FOV, covering the distance between one annulus (0.242 $R_\odot$) in 10–15 min on average. This shift corresponds to an outward propagation at an approximately constant speed of about 200–280 km s^{-1} – with a mean value of about 240 ± 40 km s^{-1} – in the hypothesis that the motion takes place entirely on the POS. Hence, the measured values are lower limits of the actual outward speed of the coronal structures. The available data do not show any detectable acceleration in the motion of the density structures.

According to previous studies, at a given heliocentric distance, the propagation speed of the coronal density fluctuations may vary in a wide range. During a solar minimum, in the range from 1.5 to 3.5 $R_\odot$, Jones & Davila (2009) reported a mean speed of about 240 km s^{-1} deduced from a speed distribution of more than 400 events based on STEREO/COR1 observations. Based on synergetic observations with various instruments on board the STEREO satellite, Alzate et al. (2021) were able to track outflowing small-scale features originating to within tenths of a solar radius from the Sun's surface moving with velocities progressively increasing from 30 km s^{-1} up to 100 km s^{-1} from 1.2 $R_\odot$ out to 4 $R_\odot$, respectively. In the range from 2.5 to 15 $R_\odot$, the outward speed was found to vary from 90 km s^{-1} to 200 km s^{-1} (Viall & Vourlidas 2015; Alzate et al. 2021). Values of about 200 km s^{-1} were detected near 10 $R_\odot$ during solar maximum, with clear evidence of acceleration to speeds of up to 400 km s^{-1} at about 13 $R_\odot$ (DeForest et al. 2018). In the case of the coronal blobs, which have been continuously observed for more than two solar cycles during the SOHO mission, the outflow speed of the plasmoids – detaching in the form of magnetic flux ropes at the cusp of helmet streamers in a limited number (four to six per day) and propagating along the plasma sheet (within ±5° from the sheet) – is spread over a broad range of values. On average, the speed varies from 150 km s^{-1} near 5 $R_\odot$ to 300 km s^{-1} at 25 $R_\odot$ (Sheeley et al. 1997, 2009; Wang 2012).

The rate of expansion of the ambient solar wind was also measured in the corona in the absence of detectable tracers, such as density inhomogeneities and blobs. This was done by simply combining the polarized visible-light and ultraviolet observations of the neutral hydrogen emission, as obtained with Metis, in order to study the Doppler dimming (see, e.g., Withbroe et al. 1982; Noci et al. 1987), that is, the intensity reduction of the neutral hydrogen emission occurring in the expanding coronal plasma. During the observational run under study, however, the ultraviolet channel of Metis was switched off; thus, it is not possible to derive the outflow velocity of the ambient slow solar wind via Doppler dimming. Nonetheless, since the west limb corona observed on February 22, 2021, was still in quiescent conditions and was mainly characterized by the coronal segment of the heliospheric current sheet roughly lying in the equatorial plane (Figs. 3 and 4), it is reasonable to compare the wind speed obtained in this section on the basis of the transient density structures with the speed of the ambient slow wind measured at solar minimum in May 2020. According to the Doppler dimming analysis of the data obtained in May 2020, between 3.8 and 7 $R_\odot$, the

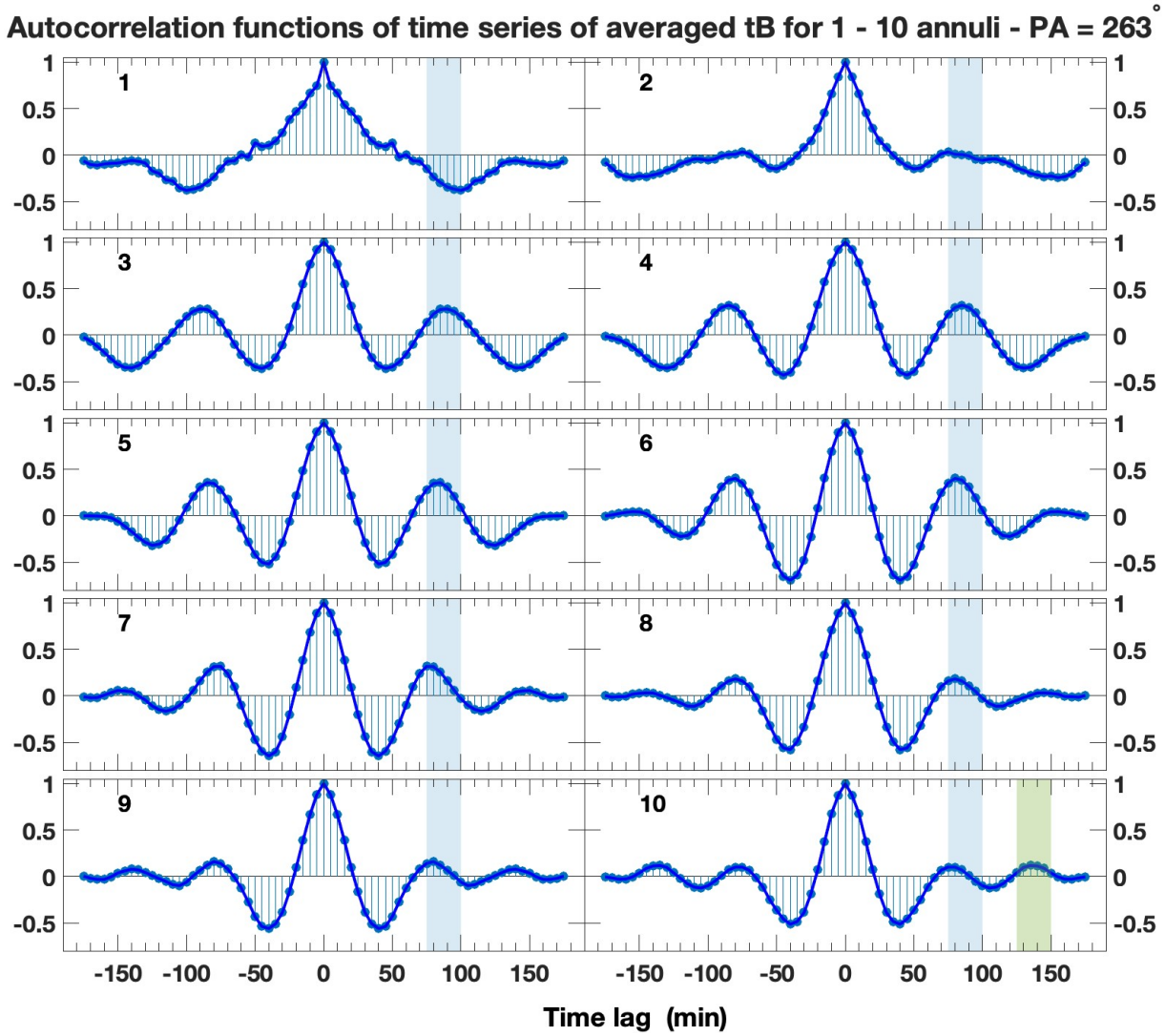

Fig. 6. Autocorrelation functions of the time series of the visible-light total brightness relating to each annulus at PA = 263°. The lag values refer to the time lag being considered. In each panel, the corresponding annulus identification number is reported in the top left. A light blue shaded area highlights the interval of 75–100 min where all the autocorrelation functions (except that obtained for annulus 1) exhibit a secondary maximum. In the bottom-right panel, referring to the annulus 10, a light green shaded area highlights the interval of 125–150 min where the autocorrelation function exhibits its third maximum.

slow wind is confined in a zone ±30° wide across the coronal current sheet (Antonucci et al. 2023), where the lowest wind is flowing along the equatorial plasma sheet coincident with the current sheet, with values varying from about 115 km s^{-1} at 4 $R_\odot$ to 150–190 km s^{-1} at 6.8 $R_\odot$ (the second value was derived in the hypothesis of isotropic velocity distribution of protons along and across the magnetic field and represents the velocity higher limit). At about ±15° from the equator, just outside the current sheet, the Doppler dimming analysis yielded an increased flow speed value of about 175–230 km s^{-1} at 6.8 $R_\odot$, depending on the hypothesis assumed for the velocity distribution of the protons relative to the magnetic field. Moreover, along both the current sheet and in the surrounding layers, there is evidence for plasma acceleration across the FOV.

4. Discussion

Summarizing the main results of the analysis presented in this paper, it can be stated that plasma is released in frequent quasi-periodic recurrent events, with a most probable cadence of 80 min, in the form of enhanced density structures propagating outward in a wide latitudinal region approximately ranging from 15° N to 30° S with respect to the Sun equator. The plasma release is well observed at the west limb, where no transient large-scale phenomena, such as the CME occurring at the east limb, were taking place at the time of the observation. The region where the propagation of the enhanced-density plasmoids occurs includes the heliospheric current sheet originating at the cusp of the almost equatorial streamer at PA = 275° (Fig. 3) and is delimited in the southern hemisphere by the plasma sheet originating from the southern pseudostreamer at PA = 236°.

The MHD simulations allowed us to define in detail the magnetic context of the coronal region interested by the release of such periodic structures. Figure 9 shows the open magnetic flux map. The red and blue colors indicate positive and negative field lines, respectively, mapped from 1.0 to 3.0 $R_\odot$. We chose 3.0 $R_\odot$ as the higher limit for the magnetic mappings because this is just below the inner FOV of Metis. The vertical line indicating the position of the west limb is approximately aligned with the mid-latitude extensions of both the northern and southern

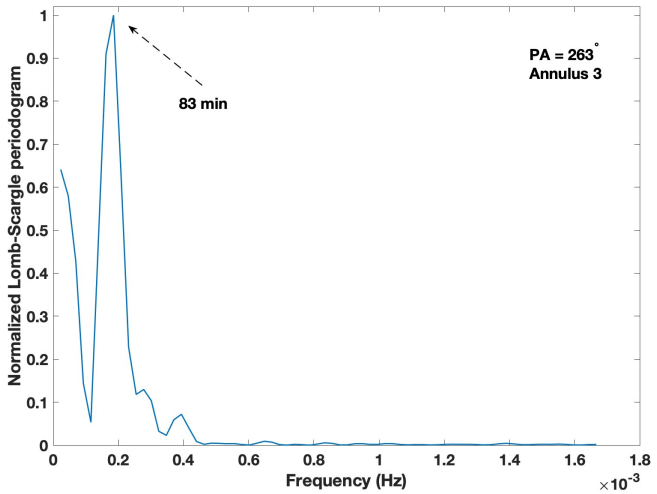

Fig. 7. Normalized Lomb-Scargle periodogram of the time series referring to annulus 3 (3.62–3.84 $R_\odot$) and PA = 263°. The period corresponding to the maximum power is indicated by an arrow.

coronal holes (Fig. 9). The signed logarithm of the squashing factor – slog Q (Titov et al. 2009) – was computed by mapping field lines from the inner boundary of the MHD model to 3 $R_\odot$, and it indicates where the separatrix and quasi-separatrix layers are located and the thickness of the web formed by the separatrix layers. Figure 10 shows slog Q at 3.0, which reveals the S-web structure just below the Metis FOV.

These results confirm that at the west limb, the heliospheric current sheet runs nearly parallel and close to the equator along the bright coronal feature, which is an extension in the outer corona of the helmet streamer (Fig. 3), and it acts as a boundary separating the solar wind emanating from the northern and southern coronal holes. This current sheet acts as a boundary, separating the solar wind emanating from the northern and southern coronal hole extensions. The S-web arc parallel to the HCS positioned at 30° south of the equator highlights the presence of a pseudostreamer giving origin to the plasma sheet seen as the bright wide feature at PA = 236° in Figs. 3 and 4. Hence, the region where the enhanced density structures are launched into the slow solar wind is associated with a complex S-web where reconnection processes along the separatrix and quasi-separatrix layers are expected to occur.

The enhanced density inhomogeneities away from the Sun appear in the form of elongated structures with a maximum total brightness about 22 to 24 times greater than the background slow wind emission level, with a spatial scale on the order of 0.7 $R_\odot$ and 0.06 $R_\odot$ in the radial direction and across the radial direction, respectively.

An interrelation among the main properties of the coronal density structures emerged from the present analysis. For example, the brighter the density structures, the longer the lifetime and more stable the shape and dimensions are while they travel toward the outer edge of the FOV. The coronal features showing a lower brightness contrast do change significantly regarding shape and dimensions, eventually elongating and fraying, and in some cases fading away 75–80 min after their appearance at the lower edge of the coronagraph FOV. Similar properties were also reported in DeForest et al. (2016).

Throughout this Metis observation, the coronal transients were released during episodic events that did not occur exactly at the same time at all the latitudes involved in the phenomenon, as reported by Sanchez-Diaz et al. (2017), for instance. However, in that case, the authors analyzed the corona during the maximum of solar activity, and the coronal segment of the heliospheric current sheet was highly tilted with respect to the equator. Therefore, the simultaneity of the ejection of plasmoids can be related to a release occurring along a sizable segment of the tilted current sheet. Moreover, the structures reported in Sanchez-Diaz et al. (2017) are significantly different from the ones analyzed in the present work, both in size (15 $R_\odot$ – 5 $R_\odot$) and timescale (≃19. 5 h).

A previous study of a long time series of Lyα observations, acquired with the Ultraviolet Coronagraph Spectrometer (UVCS; Kohl et al. 1995) at 1.7 $R_\odot$ in low-latitude streamers and in regions where the slow solar wind is typically generated and accelerated, has revealed the existence of large-scale density fluctuations only in the range of 3×10^{-6}–9×10^{-5} Hz (Telloni et al. 2009). At higher frequencies, the power spectra flatten out, suggesting that they are produced only by uncorrelated noise fluctuations. The lack of significant peaks in the frequency range corresponding to the cadence of release of the density structures in the present study might imply that the lower bound of the source location of the process responsible for quasi-periodic density structure ejection could be placed at a heliocentric distance higher than 1.7 $R_\odot$. Future works based on observations with a more advantageous FOV might clarify this point.

The density structures propagate outward at speeds on the order of 200–280 km s^{-1}, in agreement with previous results (e.g., Jones & Davila 2009; López-Portela et al. 2018). They are clearly formed in the regions where the slow solar wind originates during low solar activity and ejected at a heliocentric distance at or below 3.14 $R_\odot$ – the inner edge of the Metis FOV. In the limited FOV ranging from 3.1 to 5.7 $R_\odot$, no acceleration is detectable, whereas several works based on STEREO and SOHO/LASCO (Large Angle and Spectrometric COronagraph; Brueckner et al. 1995) observations – covering a wide range of heliocentric distances from 1.5 to about 15 $R_\odot$ – report accelerations from 1.0 to 20 m s^{-2} (see e.g., Jones & Davila 2009; Viall & Vourlidas 2015; DeForest et al. 2018). The outward speed of the observed plasmoids turned out to be higher than the typical value of the ambient solar wind at the same heights, as measured by applying the Doppler dimming technique to Metis observations during the solar activity minimum, which in turn is consistent with the speed of the coronal blobs observed with LASCO. This suggests that the density structures can be ejected at velocities higher than that of the ambient solar wind regulated by the expansion factor of the magnetic field lines and reach the slow wind velocity further out. Further investigations will be devoted to exploring whether the measured flow speeds can be related to the energy involved in the process generating the propagating structures.

We suggest that some of the features observed with Metis are associated with the switchback phenomenon revealed with the instruments of the Parker Solar Probe (PSP; Fox et al. 2016) when approaching the Sun (Bale et al. 2019). We believe that the results presented in this work, while extending the knowledge of the characteristics of these coronal features, provide further arguments in favor of the interchange reconnection interpretation advanced in Telloni et al. (2022). Indeed, the features of the wave-shaped plasmoids – which appear to move in a non-radial direction and which sometimes fray and even dissolve (see Fig. 11) – are in contrast to the characteristics of ordinary circular-shaped plasmoids and seem to be compatible with switchback phenomena. Based on the Alfvén theorem, the "S"

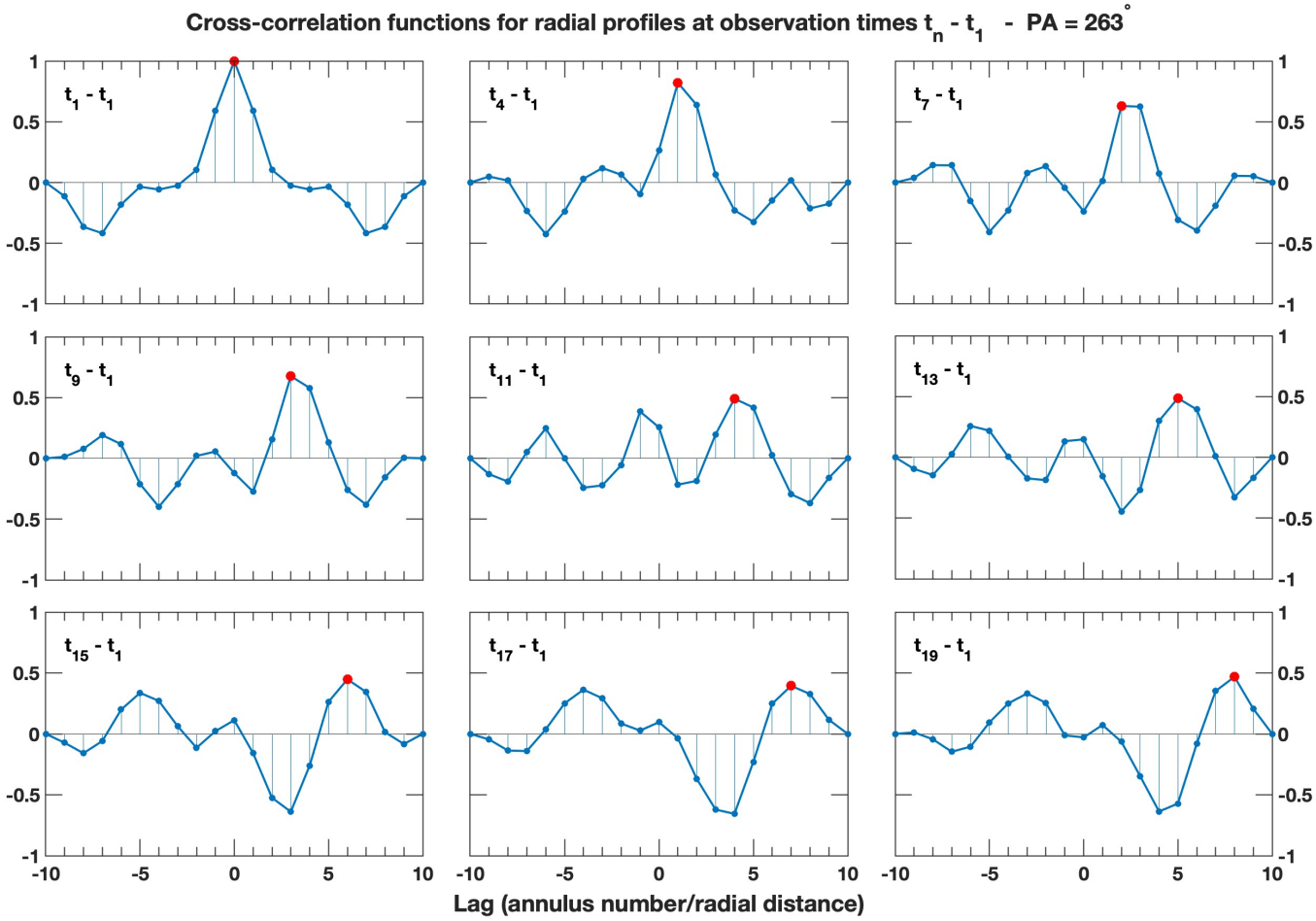

Fig. 8. Cross-correlation functions of total brightness radial series at PA = 263° for some of the successive observation instants, labeled as t_n. The lag value corresponds to the annulus position gap considered. The top-left panel shows the autocorrelation function of the radial series obtained at the instant t_1. In the other panels, the cross-correlation functions between the radial series at instant t_n and the radial series at instant t_1 are reported. In each panel, the two instants at which the cross-correlated radial series have been collected are indicated in the top left. The red point in each panel highlights the maximum value of the cross-correlation function.

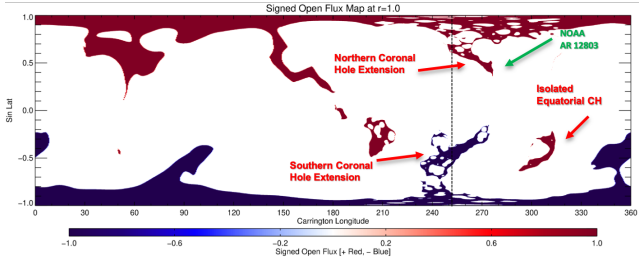

Fig. 9. Signed open magnetic flux map at 1.0 $R_\odot$ showing the equatorial extensions of the coronal holes in the vicinity of the west limb as seen by Metis (vertical line). The open magnetic field lines were computed from the inner radius (1.0 $R_\odot$) to the outer radius of the mapping (3.0 $R_\odot$). The indented appearance of the coronal hole extensions is due to low-lying closed structures formed by the presence of parasitic polarities in the radial magnetic field map.

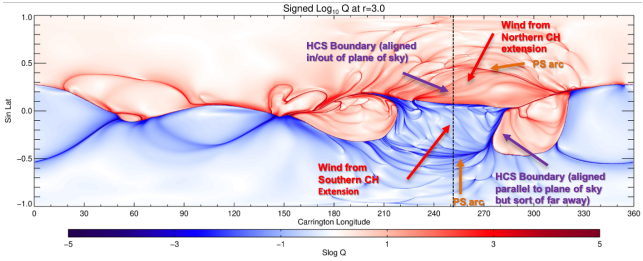

Fig. 10. Map of the signed squashing factor, signed log Q, computed at 3 $R_\odot$. The helmet streamer- heliospheric current sheet (HCS) is aligned in and out of the POS. Strong arcs at ±30° (±0.5 sin latitude) from the Sun equator indicate the signature of the large-scale pseudostreamers. The wind along the field lines rooted in the northern and southern coronal holes extensions spans the zone ±30° from the equator.

shape of the switchback-related magnetic field should also be observed in the plasma and, in turn, in the coronal total brightness images obtained with Metis. These peculiar plasmoids were observed to form in the vicinity of the heliospheric current sheet, at about 3 $R_\odot$, that is, at the coronal level where interchange reconnection is expected to develop (Zank et al. 2020). We note that their periodicity – ranging between 1 and 2 h – would provide information about the timescale at which interchange reconnection occurs. This timescale is in agreement with the duration of the supergranular-scale micro-streams observed by Bale et al. (2022) and interpreted as being driven by interchange reconnection. Most interestingly, switchbacks clearly occur in clusters, which is consistent with the expectations for interchange

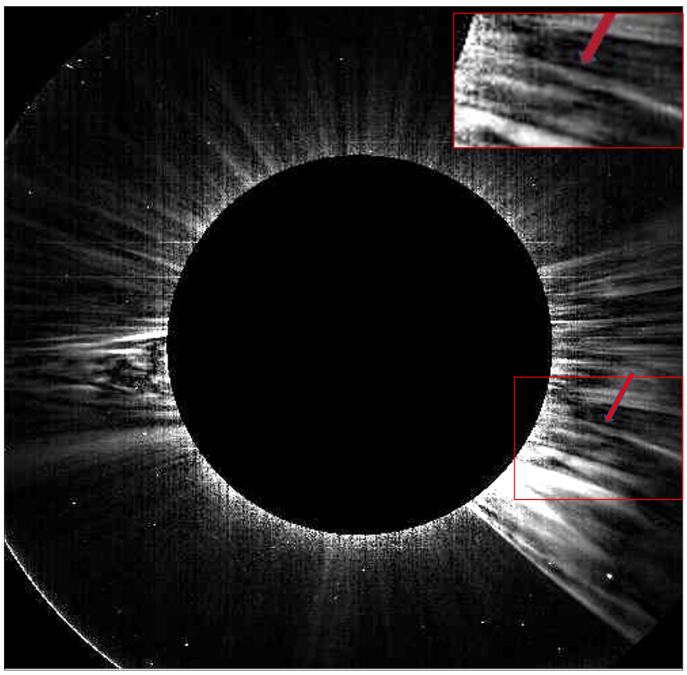

Fig. 11. Total brightness image of the solar corona acquired with the Metis coronagraph on February 22, 2021, at 20:55 UT. This observation caught one example of the wave-shaped plasmoids, which were detected while propagating in the FOV of the coronagraph at PA ≃250°, compatible with the switchback phenomenon. The inset panel presents a zoom of the region bordered in red in the larger figure. A movie of the full frames of the Metis observation sequence, available online, shows the phenomenon more clearly.

reconnection. The first direct imaging of a magnetic switchback in the solar corona with Metis (Telloni et al. 2022) unveiled the coronal origin of switchbacks, allowing for the identification of the interchange reconnection as the most probable formation mechanism. The observation of switchbacks is especially relevant because they are expected to play a key role in plasma heating and subsequent solar wind acceleration. Interchange reconnection is expected to launch switchbacks (Zank et al. 2020) and drive bursts of high-speed streams (Bale et al. 2022). Clusters of switchbacks are expected to occur in sequence with timescales related to the motion of the open magnetic flux.

At present, the central question in order to fully understand switchback formation and sources remains whether they are driven in the solar atmosphere or generated in the solar wind. In order to effectively interpret the observed plasmoids as the plasma counterpart of magnetic switchbacks, we intend to carry out an analysis of Metis-Solar Orbiter and PSP data in a future work. At present, we can conclude that the properties highlighted in this work are consistent with a switchback description of the phenomenon and interchange reconnection as the most viable mechanism underlying their generation.

5. Conclusions

The Metis observations reported here are a first demonstration of the instrument's capability to detect and monitor intermittent, quasi-periodic small-scale plasma density structures propagating through the solar corona. From this first Metis observation of density structures, we can derive the following conclusions. The release in the solar corona of frequent small-scale structures characterized by enhanced density, almost uniformly distributed at the mid and low latitudes in the vicinity of the heliospheric current sheet, can be associated with latitudes that are also the site of the thick and complex web of separatrix and quasi-separatrix layers where the process of magnetic reconnection is expected to take place. This scenario is consistent with recent observations by Chitta et al. (2023). According to our results, the release of the observed density enhancements take place at or below 3.14 $R_\odot$, the inner edge of the coronagraph FOV. The quasi-periodicity, with a frequency spectrum peaking at about 80 min, is consistent with the previous observations of density fluctuations obtained observing the corona and the slow wind in the heliosphere (see e.g., Viall & Vourlidas 2015; Kepko et al. 2016).

Some of the density structures discussed in this paper emerging from the S-web characterizing the inner corona display properties suggesting that they can be interpreted as switchbacks formed during the interchange reconnection between closed and open magnetic field lines. Switchbacks, which were proposed by Fisk & Schwadron (2001) as a mechanism to transport open magnetic flux through the corona, are characterized by a local reversal of the radial magnetic field. According to Metis observations, when coupled with PSP in situ measurements, switchbacks formed near the solar surface can maintain their shape as they propagate through the corona out to the orbit of PSP, as shown by Telloni et al. (2022). Recently, Huang et al. (2023) report evidence for the braiding of magnetic fields within the switchbacks, and according to their study, such braiding ensures that the "S" shape of these features can be maintained during propagation across the corona.

The observed enhanced density structures were ejected with a velocity that is significantly higher than the ambient slow wind velocity deduced from Metis observations during the solar minimum when applying the Doppler dimming technique – the latter providing a velocity consistent with the speed measured on the basis of the motions of tracers, such as the coronal blobs discovered by LASCO and flowing along the inner coronal part of the heliospheric current sheet. Therefore, we suggest that the speed of the density enhancement is determined by the energetics of the reconnection process itself and can be, in some if not all cases, significantly higher than the ambient solar wind speed that is instead regulated by the divergence of the coronal magnetic field lines. The absence of acceleration observed across the coronagraph FOV suggests that the plasmoids are progressively reaching the expansion rate of the ambient wind.

In conclusion, the observations analyzed in this paper are in favor of the emission of quasi-periodic enhanced-density plasmoids in the reconnection phenomena occurring in the complex web of separatrix and quasi-separatrix layers. Moreover, there is evidence based on the structural characteristics of some of the observed plasmoids that suggests the presence of switchbacks that originate during interchange reconnection processes occurring at or below 3.14 $R_\odot$ in the S-web. The fact that the speed of the plasma ejected in the reconnection process is higher than that of the ambient slow solar wind is likely to be related to the energy involved in the process generating the propagating structures.

New images acquired by Metis during the perihelion phase of October 2022 with a temporal resolution of 2 min and a more extended observation time of 10 h are presently under analysis. These images will provide an opportunity to better understand the reported phenomenon, as they have a spatial resolution of about 4000 km, which allows for a study of the propagating density inhomogeneities using images with never-before-reached detail of the outer corona acquired by

spacecrafts. The observations will also provide better insight on coronal layers in a range of heliocentric distance previously explored by the STEREO/COR1 coronagraph (Jones & Davila 2009; Alzate et al. 2021, 2023) thanks to the higher spatial and temporal resolutions of the Metis observations. This should allow accurate determination of the height where the release of the intermittent small-scale structures takes place and the speed at which the plasma is ejected during reconnection. In addition, the study of the inner layers is expected to cast light on the nature of the plasmoids and is likely to identify the source of switchbacks. A prolonged observation of such phenomena should also allow an accurate estimation of the mass contribution to the slow wind.

Acknowledgements. Solar Orbiter is a space mission of international collaboration between ESA and NASA, operated by ESA. Metis has been built and is operated with funding from the Italian Space Agency (ASI), under contracts to the National Institute of Astrophysics (INAF) and industrial partners. Metis has been built with hardware contributions from Germany (Bundesministerium für Wirtschaft und Energie through DLR), from the Czech Republic (PRODEX) and from ESA.

References

Abbo, L., Ofman, L., Antiochos, S. K., et al. 2016, Space Sci. Rev., 201, 55
Alzate, N., Morgan, H., Viall, N., & Vourlidas, A. 2021, ApJ, 919, 98
Alzate, N., Morgan, H., & Di Matteo, S. 2023, ApJ, 945, 116
Andretta, V., Bemporad, A., De Leo, Y., et al. 2021, A&A, 656, L14
Antiochos, S. K., Mikić, Z., Titov, V. S., Lionello, R., & Linker, J. A. 2011, ApJ, 731, 112
Antiochos, S. K., Linker, J. A., Lionello, R., et al. 2012, Space Sci. Rev., 172, 169
Antonucci, E., Abbo, L., & Telloni, D. 2012, Space Sci. Rev., 172, 5
Antonucci, E., Harra, L., Susino, R., & Telloni, D. 2020a, Space Sci. Rev., 216, 117
Antonucci, E., Romoli, M., Andretta, V., et al. 2020b, A&A, 642, A10
Antonucci, E., Downs, C., Capuano, G. E., et al. 2023, Phys. Plasmas, 30, 022905
Bale, S. D., Badman, S. T., Bonnell, J. W., et al. 2019, Nature, 576, 237
Bale, S. D., Drake, J. F., McManus, M. D., et al. 2022, Nature, 618, 252
Boe, B., Habbal, S., Downs, C., & Druckmüller, M. 2021, ApJ, 912, 44
Boe, B., Habbal, S., Downs, C., & Druckmüller, M. 2022, ApJ, 935, 173
Brueckner, G. E., Howard, R. A., Koomen, M. J., et al. 1995, Sol. Phys., 162, 357
Buergi, A., & Geiss, J. 1986, Sol. Phys., 103, 347
Chitta, L. P., Seaton, D. B., Downs, C., DeForest, C. E., & Higginson, A. K. 2023, Nat. Astron., 7, 133
Cranmer, S. R., Gibson, S. E., & Riley, P. 2017, Space Sci. Rev., 212, 1345
DeForest, C. E., Matthaeus, W. H., Viall, N. M., & Cranmer, S. R. 2016, ApJ, 828, 66
DeForest, C. E., Howard, R. A., Velli, M., Viall, N., & Vourlidas, A. 2018, ApJ, 862, 18
Di Matteo, S., Viall, N. M., Kepko, L., et al. 2019, J. Geophys. Res. (Space Phys.), 124, 837
Domingo, V., Fleck, B., & Poland, A. I. 1995, Sol. Phys., 162, 1
Fineschi, S., Naletto, G., Romoli, M., et al. 2020, Exp. Astron., 49, 239
Fisk, L. A., & Schwadron, N. A. 2001, ApJ, 560, 425
Fox, N. J., Velli, M. C., Bale, S. D., et al. 2016, Space Sci. Rev., 204, 7
Gershkovich, I., Lepri, S. T., Viall, N. M., Di Matteo, S., & Kepko, L. 2022, ApJ, 933, 198
Gloeckler, G., Zurbuchen, T. H., & Geiss, J. 2003, J. Geophys. Res. (Space Phys.), 108, 1158
Huang, J., Kasper, J. C., Fisk, L. A., et al. 2023, ApJ, submitted [arXiv:2301.10374]
Jones, S. I., & Davila, J. M. 2009, ApJ, 701, 1906
Kaiser, M. L. 2005, Adv. Space Res., 36, 1483
Kepko, L., Viall, N. M., Antiochos, S. K., et al. 2016, Geophys. Res. Lett., 43, 4089
Kepko, L., Viall, N. M., & Wolfinger, K. 2020, J. Geophys. Res. (Space Phys.), 125
Kohl, J. L., Esser, R., Gardner, L. D., et al. 1995, Sol. Phys., 162, 313
Lemen, J. R., Title, A. M., Akin, D. J., et al. 2012, Sol. Phys., 275, 17
Liberatore, A., Fineschi, S., Casti, M., et al. 2023, A&A, 672, A14 (SO Nominal Mission Phase SI)
Lionello, R., Linker, J. A., & Mikić, Z. 2009, ApJ, 690, 902
López-Portela, C., Panasenco, O., Blanco-Cano, X., & Stenborg, G. 2018, Sol. Phys., 293, 99
McComas, D. J., Bame, S. J., Barker, P., et al. 1998, Space Sci. Rev., 86, 563
McComas, D. J., Ebert, R. W., Elliott, H. A., et al. 2008, Geophys. Res., 35, L18103
Mikić, Z., Downs, C., Linker, J. A., et al. 2018, Nat. Astron., 2, 913
Müller, D., St. Cyr, O. C., Zouganelis, I., et al. 2020, A&A, 642, A1
Noci, G., Kohl, J. L., & Withbroe, G. L. 1987, ApJ, 315, 706
Réville, V., Velli, M., Rouillard, A. P., et al. 2020, ApJ, 895, L20
Rochus, P., Auchère, F., Berghmans, D., et al. 2020, A&A, 642, A8
Romoli, M., Antonucci, E., Andretta, V., et al. 2021, A&A, 656, A32
Sanchez-Diaz, E., Rouillard, A. P., Davies, J. A., et al. 2017, ApJ, 851, 32
Scargle, J. D. 1982, ApJ, 263, 835
Scherrer, P. H., Schou, J., Bush, R. I., et al. 2012, Sol. Phys., 275, 207
Sheeley, N. R., Wang, Y. M., Hawley, S. H., et al. 1997, ApJ, 484, 472
Sheeley, N. R., Walters, J. H., Wang, Y. M., & Howard, R. A. 1999, J. Geophys. Res., 104, 24739
Sheeley, N. R. J., Lee, D. D. H., Casto, K. P., Wang, Y. M., & Rich, N. B. 2009, ApJ, 694, 1471
Song, H. Q., Chen, Y., Liu, K., Feng, S. W., & Xia, L. D. 2009, Sol. Phys., 258, 129
Telloni, D., Antonucci, E., Bruno, R., & D'Amicis, R. 2009, ApJ, 693, 1022
Telloni, D., Zank, G. P., Stangalini, M., et al. 2022, ApJ, 936, L25
Thompson, W. T., Davila, J. M., Fisher, R. R., et al. 2003, in Innovative Telescopes and Instrumentation for Solar Astrophysics, eds. S. L. Keil, & S. V. Avakyan, SPIE Conf. Ser., 4853, 1
Titov, V. S., Forbes, T. G., Priest, E. R., Mikić, Z., & Linker, J. A. 2009, ApJ, 693, 1029
Viall, N. M., & Borovsky, J. E. 2020, J. Geophys. Res. (Space Phys.), 125, e26005
Viall, N. M., & Vourlidas, A. 2015, ApJ, 807, 176
Viall, N. M., Spence, H. E., Vourlidas, A., & Howard, R. 2010, Sol. Phys., 267, 175
Viall, N. M., DeForest, C. E., & Kepko, L. 2021, Front. Astron. Space Sci., 8, 139
Wang, Y. M. 2012, Space Sci. Rev., 172, 123
Wang, Y. M. 2020, ApJ, 904, 199
Wang, Y. M., Sheeley, N. R., J., Walters, J. H., , et al. 1998, ApJ, 498, L165
Wang, Y. M., Sheeley, N. R., Socker, D. G., Howard, R. A., & Rich, N. B. 2000, J. Geophys. Res., 105, 25133
Withbroe, G. L., Kohl, J. L., Weiser, H., & Munro, R. H. 1982, Space Sci. Rev., 33, 17
Wuelser, J. P., Lemen, J. R., Tarbell, T. D., et al. 2004, in Telescopes and Instrumentation for Solar Astrophysics, eds. S. Fineschi, & M. A. Gummin, SPIE Conf. Ser., 5171, 111
Zank, G. P., Nakanotani, M., Zhao, L. L., Adhikari, L., & Kasper, J. 2020, ApJ, 903, 1
Zurbuchen, T. H., Hefti, S., Fisk, L. A., Gloeckler, G., & von Steiger, R. 1999, Space Sci. Rev., 87, 353
Zurbuchen, T. H., Fisk, L. A., Gloeckler, G., & von Steiger, R. 2002, Geophys. Res. Lett., 29, 1352